International Journal of Science and Technology (IJST)
ISSN: 3049-1118, Volume- 3, Issue- 3 (July - September 2026)

Composition-Controlled Structural, Optical, Photoluminescence and Magnetic Properties of $Ni_xMn_{1-x}Fe_2O_4$ Nanoparticles Synthesized by Co-precipitation

Bhabataran Bhakat[1]*, Dr. Manoranjan Bar[2]
[1]Research Scholar, Department of Physics, Sona Devi University, Ghatsila, Jharkhand, India
[2]Assistant Professor, Department of Physics, Sona Devi University, Ghatsila, Jharkhand, India

Abstract

A composition series of $Ni_xMn_{1-x}Fe_2O_4$ nanoparticles (x = 0, 0.3, 0.5, 0.7 and 1.0) was investigated to establish how Ni^{2+} substitution modifies the coupled structural, optical and magnetic behavior of manganese ferrite. The samples were prepared by co-precipitation followed by thermal treatment, and the resulting powders were examined by X-ray diffraction (XRD), Fourier-transform infrared spectroscopy (FTIR), scanning electron microscopy (SEM), energy-dispersive X-ray spectroscopy (EDX), UV-Visible spectroscopy, photoluminescence (PL) spectroscopy and vibrating sample magnetometry (VSM). XRD confirms a cubic spinel ferrite framework for all compositions, with a lattice parameter decreasing from 8.3317 Å for x = 0 to 8.3137 Å for x = 1.0, indicating lattice contraction in the Ni-rich end member. FTIR supports ferrite formation through the tetrahedral metal-oxygen vibration, which shifts from 513 to 554 cm^{-1} with increasing Ni content. SEM reveals agglomerated quasi-spherical nanoscale domains, while EDX verifies progressive replacement of Mn by Ni and cation-normalized formulas close to AB_2O_4 stoichiometry. UV-Visible Tauc analysis gives a non-monotonic direct optical band gap, increasing to 2.200 eV at x = 0.3 and then decreasing to 1.823 eV for x = 1.0. PL spectra show near-UV/violet emission around 378-382.5 nm and weaker defect-related visible emission, indicating surface and vacancy-associated recombination. VSM results show ferrimagnetic hysteresis, with the apparent high-field moment increasing toward the Ni-rich composition. The integrated results demonstrate that Ni substitution is an effective route for tailoring multifunctional spinel ferrites for optoelectronic, magnetic, sensing and photocatalytic applications.

Keywords: Ni-doped manganese ferrite, spinel ferrite, optical band gap, photoluminescence, VSM, ferrimagnetism, nanoparticle.

1. Introduction

Spinel ferrites with the general formula MFe_2O_4 are technologically important magnetic oxides because they combine chemical stability, high electrical resistivity, tunable cation distribution

*Corresponding Author Email: bhabataranbhakat@gmail.com
Published: 15 July 2026
DOI: https://doi.org/10.70558/IJST.2026.v3.i3.241313

and composition-dependent optical and magnetic response (Goldman, 2006), (Smit & Wijn, 1959). Their oxygen sublattice forms a close-packed framework, whereas metal cations occupy tetrahedral A sites and octahedral B sites. The physical properties of such ferrites are controlled not only by the nominal chemical formula but also by the distribution of divalent and trivalent cations between these sites, crystallite size, lattice strain, surface disorder and defect concentration. This makes mixed ferrite nanoparticles particularly useful for studying structure-property relationships and designing materials that can operate in optical, magnetic, catalytic, and electronic environments.

Manganese ferrite and nickel ferrite represent two important end members of the spinel ferrite family. $MnFe_2O_4$ is often considered a relatively soft ferrite with a high magnetic moment contribution from Mn^{2+}, whereas $NiFe_2O_4$ commonly displays inverse-spinel character, strong B-site preference of Ni^{2+} and significant magnetic anisotropy (Verwey & Heilmann, 1947; Goldman, 2006) When Ni^{2+} substitutes for Mn^{2+} in $Ni_xMn_{1-x}Fe_2O_4$, the replacement changes the local bond length, A-B superexchange interaction, cation redistribution and surface spin arrangement. At the nanoscale these effects become more complex because surface-to-volume ratio, spin canting, agglomeration and non-equilibrium site occupancy can modify the expected bulk trends (Chinnasamy, et al., 2001; D. & D., 2009) Therefore, a systematic composition series is necessary to separate simple composition effects from size, strain and surface effects.

Optical properties are also strongly composition-sensitive in transition-metal ferrites. The valence and conduction band edges arise from hybridized O 2p and transition-metal 3d states, while Fe^{3+}/Fe^{2+} charge transfer, Mn-related states, Ni-related crystal-field effects, oxygen vacancies and surface defects can introduce additional sub-gap absorption or radiative recombination centers. Thus, UV-Visible and PL spectroscopy provide complementary evidence: UV-Visible absorption reveals the optical absorption edge and apparent band-gap tuning; PL identifies radiative recombination pathways and defect-related emission. For ferrite nanoparticles, Tauc-derived band gaps should be interpreted comparatively because broad absorption and scattering often obscure a sharp absorption edge.

A major challenge in publishing ferrite nanoparticle research is avoiding over-interpretation of isolated parameters. A small change in lattice parameter can be physically meaningful only when supported by consistent changes in vibrational frequency, composition, and microstructure. Similarly, an apparent change in band gap should not be attributed only to quantum confinement without considering defect absorption, particle agglomeration, and baseline effects in absorbance spectra. Magnetic measurements also require caution because measured moment depends on sample mass, packing, background correction, and high-field approach to saturation. For this reason, the present manuscript explicitly states the data-treatment assumptions and uses cross-correlation as the main interpretation strategy. This approach is aligned with the requirements of high-quality journal reporting, where reproducibility, transparent limitations and consistency between independent techniques are as important as numerical trends.

The present work investigates $Ni_xMn_{1-x}Fe_2O_4$ nanoparticles with $x = 0, 0.3, 0.5, 0.7$ and 1.0 using a multi-technique approach. The objective is to correlate phase formation, metal-oxygen bonding, morphology, composition, band-gap tuning, defect emission and magnetic response.

Unlike single-technique studies, this paper treats XRD, FTIR, SEM, EDX, UV-Visible, PL and VSM as mutually connected evidence. The central hypothesis is that Ni substitution modifies the ferrite lattice and bonding environment, and that these changes propagate into the optical and magnetic behaviour through lattice contraction, site occupancy, surface defects and A-B exchange interactions.

A further motivation for studying the complete x = 0-1 series is that end-member behaviour alone cannot identify the optimum composition. A material may show the largest magnetic moment at one end of the series, while the best optical response or lowest coercive loss occurs at an intermediate composition. In real applications such as recyclable photocatalysts, magnetic sensors or optoelectronic-magnetic hybrid components, balanced performance is often more important than maximizing a single parameter. A composition map therefore provides more useful guidance than isolated single-composition characterization. The present manuscript is written from this perspective and emphasizes how the measured structural, optical, and magnetic parameters evolve together.

2. Experimental details

$Ni_xMn_{1-x}Fe_2O_4$ nanoparticles with nominal compositions x = 0, 0.3, 0.5, 0.7 and 1.0 were synthesized by an alkaline co-precipitation route. Analytical-grade nickel nitrate, manganese nitrate and ferric chloride precursors were dissolved in double-distilled water according to the required stoichiometry, maintaining the total divalent-to-ferric cation ratio appropriate for the spinel formula. Sodium hydroxide solution was added under continuous stirring to precipitate mixed metal hydroxide intermediates. The precipitate was aged, repeatedly washed to remove soluble ions, dried, ground and thermally treated about 700 ^{O}C to obtain crystalline ferrite powders. The sample codes F1, F2, F3, F4 and F5 correspond to x = 0, 0.3, 0.5, 0.7 and 1.0, respectively.

Powder XRD patterns were recorded using Cu Kα radiation and analyzed by peak fitting around the principal spinel reflections. The cubic lattice parameter was calculated from the interplanar spacing using $a = d(h^2 + k^2 + l^2)^{1/2}$, and crystallite size was estimated from the Scherrer equation $D = K\lambda/(\beta \cos\theta)$, where K = 0.9, λ = 1.5406 Å, β is the full width at half maximum in radians and θ is the Bragg angle (Cullity & Stock, 2001). Because an instrumental broadening standard was not supplied, the crystallite size and microstrain values are treated as apparent comparative parameters. FTIR spectra were recorded from 4000 to 450 cm^{-1} to identify metal-oxygen vibration bands and surface functional groups. SEM was used to evaluate morphology and agglomeration, and visible particle/domain sizes were estimated from micrographs using the scale bar. EDX was used for selected-area elemental quantification. Since oxygen is a light element and EDX oxygen quantification is less reliable than metallic-cation quantification, spinel formulas were calculated by normalizing metallic cations to three cations per AB_2O_4 formula unit.

UV-Visible spectra were processed to evaluate optical absorption behavior and apparent direct band gaps using the Tauc relation $(\alpha h\nu)^2 = B(h\nu - Eg)$. Absorbance was used as a proportional measure of α for comparative analysis under constant measurement conditions. PL emission spectra were measured in the 300–700 nm range using 280 nm excitation to identify

recombination and defect-related emission. VSM M-H curves were recorded over approximately ±16 kOe. The uploaded VSM data provide magnetic moment in emu but not sample mass; therefore, the magnetic values are reported as apparent moment rather than mass-normalized magnetization in emu g^{-1}. The coercive field Hc, remanent moment Mr, squareness ratio Mr/Ms and loop-area indicator were extracted from the hysteresis curves.

3. Results and discussion

3.1. XRD phase formation and FTIR bonding correlation

The XRD patterns shown in figure, the main spinel ferrite reflections corresponding to planes such as (220), (311), (400), (422), (511) and (440). The presence of these reflections across the full composition range confirms that the ferrite lattice is retained from the Mn-rich to the Ni-rich end member. The (311) reflection, which is typically the most intense spinel ferrite peak, was used as a principal basis for crystallite-size and lattice comparisons. The average lattice parameter varies only slightly in the intermediate region but decreases to 8.3137 Å for x = 1.0. This contraction is consistent with incorporation of Ni^{2+} into the ferrite framework and with the smaller effective size of Ni-related octahedral coordination relative to Mn-rich environments.

The apparent crystallite size from the (311) peak lies in the nanocrystalline range, varying from 19.57 nm for x = 0 to 27.15 nm for x = 0.3, 20.78 nm for x = 0.5, 15.63 nm for x = 0.7, and 19.66 nm for x = 1.0. The non-monotonic trend indicates that crystallite growth is controlled by more than ionic radius alone. Nucleation density, local supersaturation, thermal treatment, defect accumulation and cation redistribution can all influence line broadening. The minimum D(311) at x = 0.7 coincides with higher structural disorder in the Ni-rich mixed composition, indicating that intermediate substitution may generate local strain before the end-member Ni ferrite lattice is stabilized.

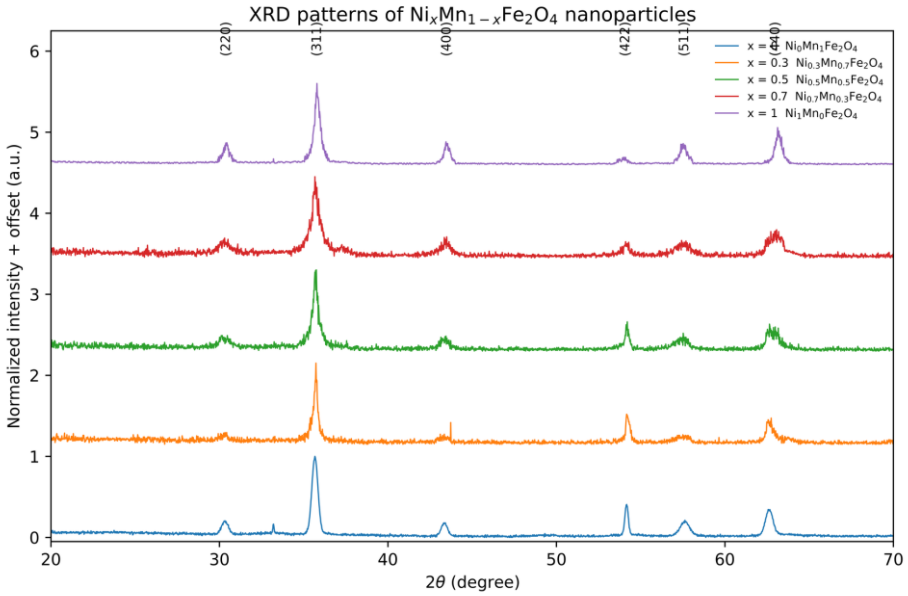

Figure 1. XRD patterns of $Ni_xMn_{1-x}Fe_2O_4$ nanoparticles showing characteristic cubic spinel reflections

FTIR results shown in figure 2 provide an independent confirmation of ferrite bond formation. The high-frequency metal-oxygen band assigned to tetrahedral-site vibration shifts from 513 cm^{-1} for x = 0 to 526, 543, 547, and 554 cm^{-1} for increasing Ni content shown in figure 3. In spinel ferrites, tetrahedral and octahedral M-O vibrations are sensitive to cation mass, bond length and force constant (Waldron, 1955). The observed shift toward higher wavenumber indicates a strengthening of the local metal-oxygen bonding environment. The lower-frequency octahedral vibration appears as an absorption edge at the lower measurement limit of 450 cm^{-1}; therefore, it is interpreted as an unresolved edge/shoulder rather than a fully resolved peak. The weak O-H and H-O-H bands indicate surface hydroxyl or adsorbed water species, which are common in oxide nanoparticles (Noei, et al., 2008; Borah, et al., 2021) and may contribute to surface states.

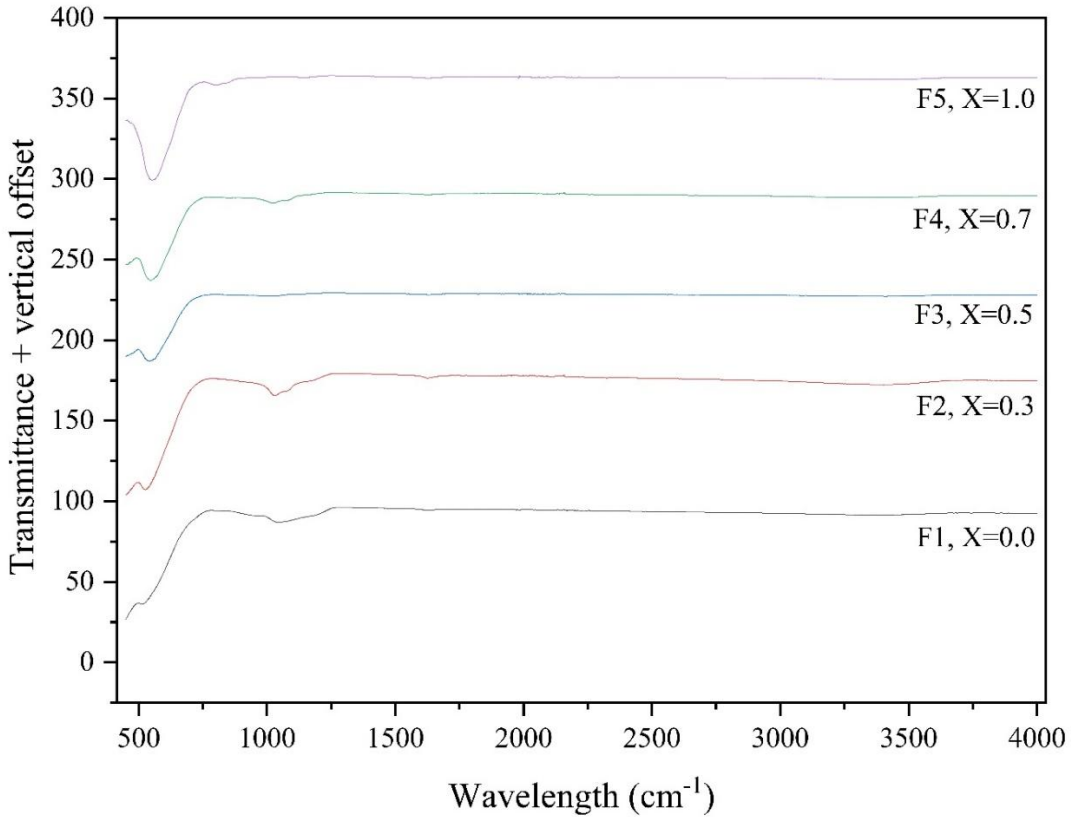

Figure 2 : FTIR Show the confirmation of ferrite bond formation

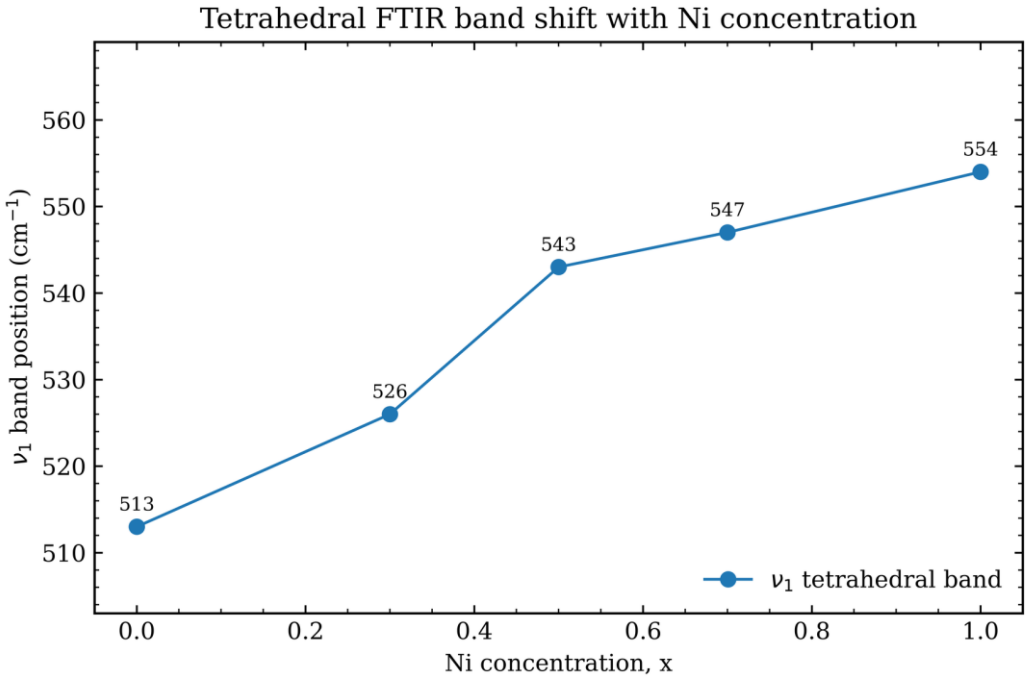

Figure 3. Shift of the tetrahedral FTIR metal-oxygen vibration band with Ni substitution.

The XRD-FTIR agreement is particularly significant because both techniques respond to different aspects of the same structural modification. XRD provides long-range periodic information through Bragg reflections (Wang L. , 2017, p. 75), while FTIR reflects short-range metal-oxygen force constants (Varsamis, Makris, Valvi, & Kamitsos, 2021, p. 10015). If Ni substitution only occurred as segregated Ni-rich impurities, the lattice contraction and systematic FTIR shift would not be expected to remain correlated across the series. The simultaneous structural contraction and vibrational hardening therefore support incorporation of Ni into the spinel framework. However, the small non-monotonic variations in intermediate compositions also suggest that the lattice is not perfectly ideal; local cation disorder, microstrain and size dispersion are present and can influence the subsequent optical and magnetic results.

3.2. Morphology and compositional verification

SEM analysis shown in figure micrographs reveal granular, agglomerated and quasi-spherical nanoparticle domains. The apparent SEM mean size increases from 25.02 nm at x = 0 to 29.19 nm at x = 0.3, 29.81 nm at x = 0.5 and 33.43 nm at x = 0.7, followed by a slight decrease to 32.18 nm for x = 1.0. These SEM values are larger than the XRD crystallite sizes, showing that the visible particles are not necessarily single coherent crystallites. Instead, the SEM domains represent agglomerated or multi-crystallite particles. This distinction is important because ferrite nanoparticles have high surface energy (Namai, et al., 2012, p. 1037) and can experience magnetic dipole-dipole interaction (Qiu, Jensen, Charity, Towner, & Mao, 2010, p. 17730), van der Waals attraction and hard aggregation (Nasirpouri, et al., 2023, p. 25145) during drying and calcination.

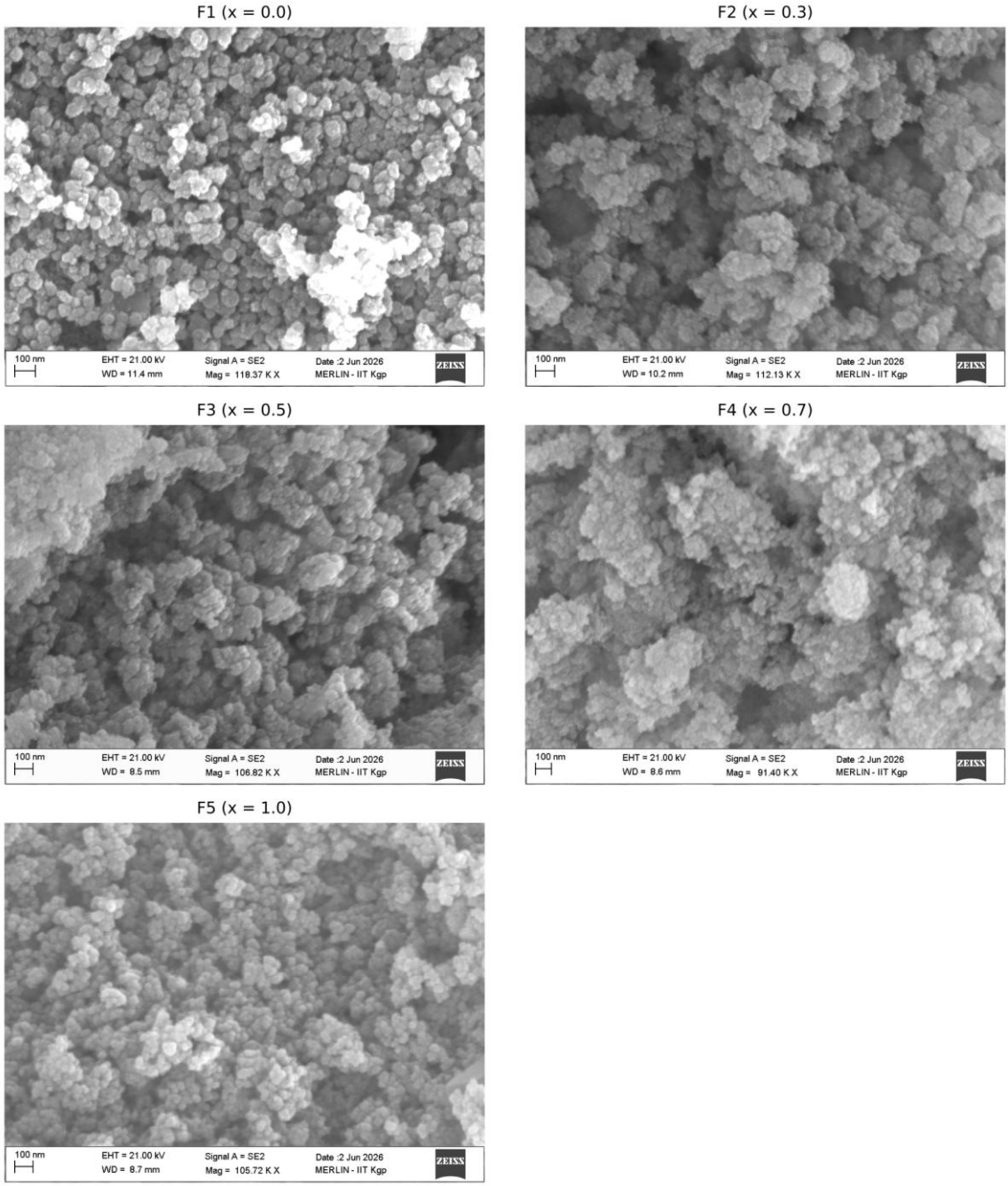

Figure 4. SEM micrographs showing agglomerated nanoscale morphology across the composition series.

The EDX data confirm the elemental presence of Mn, Ni, Fe and O in the appropriate compositions. The cation-normalized formulas are $Mn_{0.92}Fe_{2.08}O_4$ for x = 0, $Mn_{0.73}Ni_{0.30}Fe_{1.97}O_4$ for x = 0.3, $Mn_{0.51}Ni_{0.50}Fe_{1.98}O_4$ for x = 0.5, $Mn_{0.32}Ni_{0.62}Fe_{2.05}O_4$ for x = 0.7 and $Ni_{1.03}Fe_{1.97}O_4$ for x = 1.0. The gradual increase of Ni coefficient and corresponding reduction of Mn coefficient verify successful substitution. The total metallic cation coefficient remains close to three for all samples, satisfying the AB_2O_4 spinel requirement. No foreign elements are present in the quantified EDX tables, suggesting that the selected areas are chemically consistent with the target ferrite phase. The EDX oxygen values are not over-

interpreted because light-element quantification in EDX is more uncertain than metallic cation ratios (Tong & Mingard, 2026; Newbury & Ritchie, 2014)

Composition verification is central for claiming controlled doping (Buonsanti & Milliron, 2013; Chen, et al., 2009) In the present series, the EDX-derived Ni coefficient increases from zero in F1 to approximately 1.03 in F5, while the Mn coefficient decreases from 0.92 to zero. The Fe coefficient remains between 1.97 and 2.08, close to the expected ferrite value. These values confirm that the intended substitution occurs primarily on the divalent-cation sublattice rather than by major Fe deficiency or uncontrolled secondary metal enrichment. Minor deviations from ideal stoichiometry are reasonable for selected-area EDX because surface roughness (Newbury & Ritchie, 2014, p. 498), agglomeration (Small, 2002, p. 555), interaction volume (Rades, et al., 2014, p. 49582) and light-element uncertainty influence the measured atomic percentage. For a journal manuscript, the key point is therefore not exact equality with the nominal formula but the systematic and chemically meaningful trend across the full series.

3.3. UV-Visible absorption, band-gap tuning and PL response

The UV-Visible spectra show broad absorption over the UV and visible regions shown in figure 5. Such broad absorption is typical of transition-metal oxide nanoparticles because band-edge absorption overlaps with charge-transfer transitions, defect tails and scattering contributions (Manthiram & Alivisatos, 2012; Nguyen-Phan, et al., 2015). The direct Tauc analysis gives a corrected optical band gap of 2.083 eV for $MnFe_2O_4$. A higher value of 2.200 eV is obtained for x = 0.3, followed by a reduction to 2.039 eV for x = 0.5, 1.896 eV for x = 0.7 and 1.823 eV for $NiFe_2O_4$. This non-monotonic variation indicates that the optical response is controlled by competing mechanisms. The initial increase at low Ni content may arise from improved crystallinity, modification of surface states or reduced defect-tail contribution. At higher Ni content, enhanced Ni-O/Fe-O hybridization, increased density of localized states and changes in cation distribution can lower the apparent optical transition energy.

The relationship between crystallite size and band gap is not purely governed by quantum confinement (Becerril-Romero, et al., 2020; Wang, Berg, Donegá, Jong, & Jongh, 2016, p. 33689) Although nanoscale crystallites can show size-dependent optical behaviour, the measured crystallite sizes exceed the range where a simple strong-confinement model would dominate in ferrites. Therefore, the band-gap variation is better understood as a combined effect of lattice contraction, cation redistribution, defect states and electronic hybridization. The x = 0.7 and x = 1.0 samples show lower band gaps and significant visible response, making them potentially useful for visible-light-driven optoelectronic or photocatalytic applications.

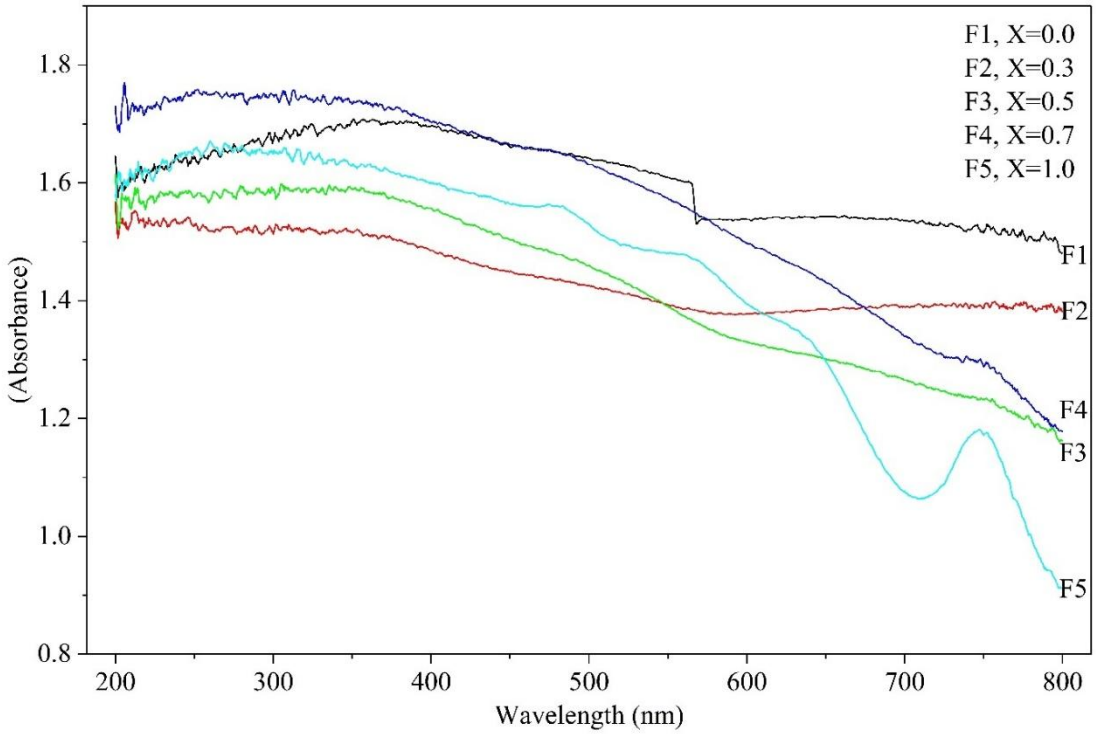

Figure 5 The UV-Visible spectra show broad absorption

The optical absorption behaviour is also affected by morphology. Agglomerated nanoparticles can enhance diffuse scattering and produce a sloping background in absorbance spectra. In addition, surface hydroxyl groups and oxygen vacancies may introduce tail states below the fundamental transition. For this reason, baseline-corrected Tauc analysis was used for comparison. The calculated Eg values should be interpreted as apparent optical transition energies rather than perfect single-crystal band gaps. This interpretation is scientifically safer and more suitable for peer review, because ferrite nanoparticles rarely exhibit a sharp direct absorption edge like a high-quality bulk semiconductor.

PL spectra measured under 280 nm excitation show a dominant near-UV/violet emission peak around 378-382.5 nm for all samples shown in figure 6, with weaker visible emission attributed to defect-related states. The global PL peak appears at 379.5 nm for x = 0, 382.5 nm for x = 0.3, 378.0 nm for x = 0.5, 380.0 nm for x = 0.7 and 379.5 nm for x = 1.0. The integrated PL intensity decreases from 2645.9 for x = 0 to 2318.1 for x = 0.3 and 2026.1 for x = 0.5, increases slightly to 2194.8 for x = 0.7 and returns to 2030.4 for x = 1.0. The reduction of PL intensity for Ni-containing samples suggests that Ni substitution introduces non-radiative recombination pathways or changes the population of radiative defect centers. The PL response supports the presence of surface defect states, oxygen-vacancy-associated recombination and cation-disorder-assisted transitions.

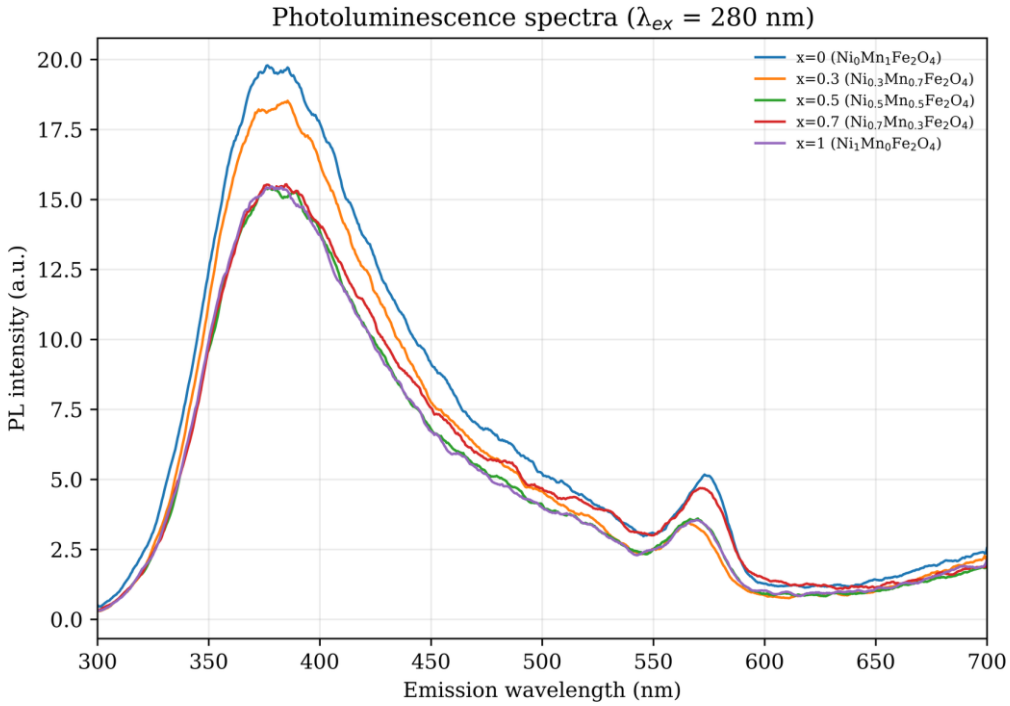

Figure 6. PL emission spectra recorded under 280 nm excitation.

3.4. Magnetic hysteresis and Ni-dependent ferrimagnetic behaviour

VSM M-H loops confirm ferrimagnetic behaviour for the $Ni_xMn_{1-x}Fe_2O_4$ series shown in figure 7. the saturation parameter is reported as apparent high-field moment in emu. The apparent Ms increases from 0.0073 emu for x = 0 to 0.1719 emu for x = 0.3, 0.3014 emu for x = 0.5, 0.5049 emu for x = 0.7 and 0.7697 emu for x = 1.0. This strong increase suggests that the Ni-rich compositions provide enhanced magnetic alignment under applied field in the measured samples. The trend is consistent with increased ferrimagnetic contribution, improved exchange connectivity and composition-dependent spin ordering.

The coercivity displays a non-monotonic trend. The Mn-rich F1 sample gives a higher apparent Hc of 281.17 Oe, while F2, F3 and F4 show much lower coercivities of 20.88, 16.42 and 15.79 Oe, respectively. This indicates soft magnetic behaviour in the mixed compositions, which is favourable for applications requiring easy magnetization reversal and low hysteresis loss. The F5 $NiFe_2O_4$ sample shows Hc = 132.66 Oe and the largest loop area. This increase is consistent with stronger effective anisotropy, higher remanence and enhanced magnetic energy dissipation in the Ni-rich sample. The squareness ratio Mr/Ms is low for F2-F4, indicating that these samples do not retain a large fraction of magnetization after field removal. F5 shows a higher squareness ratio of 0.1185, suggesting stronger magnetic retention.

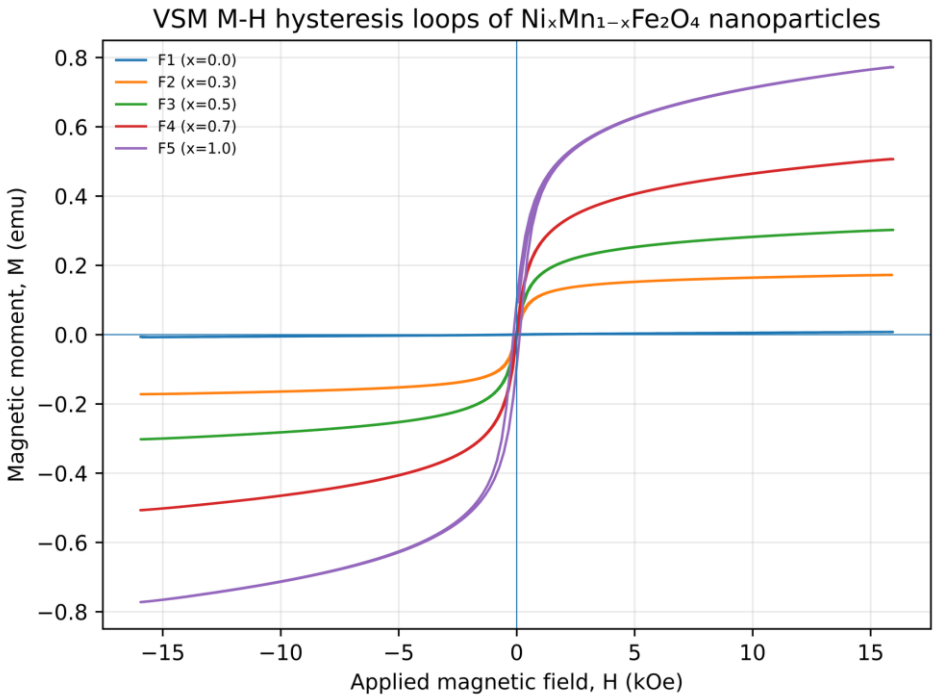

Figure 7. VSM M-H hysteresis loops confirming ferrimagnetic behaviour in the $Ni_xMn_{1-x}Fe_2O_4$ series.

Compared with ideal bulk ferrites, nanoparticle ferrites commonly show reduced remanence and altered coercivity because a large fraction of spins are located near surfaces and interfaces. Surface atoms have incomplete coordination and may experience broken exchange bonds, producing spin canting and non-collinear magnetic structure (Hellman, et al., 2017; Ziese, 2002, p. 16) Agglomeration can either strengthen interparticle magnetic coupling or create randomly oriented clusters that reduce remanent alignment. The low Mr/Ms values of the mixed compositions indicate that magnetization can be reversed easily and that the particles do not behave as strongly square, hard magnetic materials. Such behaviour is advantageous for low-loss magnetic applications, but for biomedical or colloidal use further tests such as zero-field-cooled/field-cooled magnetization and dynamic relaxation would be required.

The magnetic trends can be interpreted through cation distribution and A-B superexchange. In spinel ferrites, the net ferrimagnetic moment is the difference between the magnetic moments of the B and A sublattices, and the strongest exchange interaction is usually the A-O-B superexchange pathway (Magnetism and the chemical bond, 1963; Néel, 1948) Ni^{2+} commonly prefers octahedral B sites, while Mn^{2+} and Fe^{3+} distributions depend on synthesis route and particle size. As Ni increases, the balance of sublattice magnetization and anisotropy changes. Surface spin disorder and agglomeration further influence the measured hysteresis. The larger SEM particle domains and stronger agglomeration in Ni-rich samples may also contribute to stronger interparticle magnetic coupling.

3.5. Integrated structure-property mechanism and application relevance

The combined results demonstrate a clear composition-structure-property relationship. Ni substitution contracts the lattice, shifts metal-oxygen vibrations to higher frequency, alters

particle aggregation, tunes the optical band gap, modifies defect-mediated PL intensity and changes magnetic reversal behaviour. The x = 0.3 sample shows the largest apparent direct band gap and good crystallite growth, suggesting that low Ni substitution can reduce defect-tail absorption or modify electronic transitions. The x = 0.7 and x = 1.0 compositions show narrower band gaps and stronger magnetic response, making them attractive for multifunctional applications where visible-light absorption and magnetic recovery are both useful.

For photodetector and photocatalytic applications, broad visible absorption and defect-assisted charge separation are beneficial, but excessive defects can also increase recombination. The Ni-rich samples may therefore provide stronger light absorption, while intermediate compositions may offer a better balance between charge generation and recombination. For magnetic applications such as sensors, electromagnetic interference shielding and magnetic separation, the measured soft ferrimagnetic behaviour of the mixed compositions is useful because low coercivity enables fast response. The high moment and higher loop area of $NiFe_2O_4$ may be useful where stronger magnetic retention or energy dissipation is desired.

From an application viewpoint, different compositions serve different functions. The x = 0.3 sample is attractive when a relatively wider optical gap and lower magnetic loss are desired. The x = 0.7 sample combines reduced optical gap, low coercivity and high apparent moment, making it suitable for magnetic-assisted visible-light processes. The x = 1.0 sample provides the strongest apparent magnetic response and narrower optical gap, but its higher coercivity and loop area imply greater magnetic energy loss. Thus, the optimum composition depends on whether the target application prioritizes optical absorption, magnetic recoverability, low hysteresis loss or defect-mediated surface activity. The data indicate that intermediate Ni substitution is particularly useful when balanced optoelectronic-magnetic behaviour is required.

The integrated dataset also suggests that the ferrite series should not be classified simply as an optical or magnetic material. Instead, the same compositional change that controls lattice contraction also changes electronic states and magnetic sublattice balance. This is advantageous for multifunctional material design because one synthesis variable, the Ni fraction, can be used to tune several properties simultaneously. Such coupling is useful in applications where a ferrite powder must absorb light, generate charge carriers and then be magnetically recovered from a reaction medium, or where an optically active oxide is required to retain magnetic functionality for sensing or separation.

Overall, $Ni_xMn_{1-x}Fe_2O_4$ nanoparticles behave as tunable multifunctional materials. Their performance cannot be assigned to a single descriptor such as crystallite size or Ni content alone. Instead, the observed behaviour arises from the coupled action of lattice parameter, cation distribution, metal-oxygen bond strength, agglomeration, defects and spin interactions. This integrated interpretation is important for designing ferrite nanoparticles for optoelectronic-magnetic hybrid devices.

Table 1. Optical, photoluminescence and magnetic parameters extracted from UV-Visible, PL and VSM analysis.

Sample	x	Eg (eV)	PL peak (nm)	PL integral	Ms* (emu)	Hc (Oe)	Mr/Ms
F1	0.0	2.083	379.5	2645.9	0.0073	281.17	0.0448
F2	0.3	2.200	382.5	2318.1	0.1719	20.88	0.0357
F3	0.5	2.039	378.0	2026.1	0.3014	16.42	0.0210
F4	0.7	1.896	380.0	2194.8	0.5049	15.79	0.0175
F5	1.0	1.823	379.5	2030.4	0.7697	132.66	0.1185

Ms* denotes apparent high-field magnetic moment in emu, not mass-normalized magnetization, because sample mass was not provided.

4. Conclusions

A complete composition series of $Ni_xMn_{1-x}Fe_2O_4$ nanoparticles was investigated using structural, vibrational, morphological, compositional, optical, luminescent and magnetic techniques. XRD confirms cubic spinel ferrite formation across x = 0–1, while the lattice parameter decreases toward $NiFe_2O_4$. FTIR corroborates metal-oxygen bonding and shows a systematic shift of the tetrahedral vibration from 513 to 554 cm^{-1}, indicating modification of bond strength with Ni substitution. SEM shows agglomerated nanoscale domains whose mean apparent size is larger than the XRD crystallite size, confirming multi-crystallite aggregation. EDX verifies progressive replacement of Mn by Ni and cation-normalized formulas close to the AB_2O_4 spinel requirement.

UV-Visible analysis demonstrates composition-dependent optical band-gap tuning. The direct band gap increases to 2.200 eV at x = 0.3 and then decreases to 1.823 eV for x = 1.0. PL spectra reveal near-UV/violet emission around 378-382.5 nm and weaker defect-related emission, showing that surface states and oxygen-vacancy-related centers contribute to recombination. VSM confirms ferrimagnetic hysteresis, with low coercivity in the mixed compositions and a larger apparent moment in the Ni-rich sample. The overall results show that Ni substitution provides an effective pathway for tuning structural disorder, optical absorption, defect emission and magnetic response in manganese ferrite nanoparticles. These materials are promising for optoelectronic, photocatalytic, magnetic sensing, EMI shielding and magnetic separation applications, provided that future studies optimize particle dispersion, mass-normalized magnetization and device-level performance.

Declarations

Funding: No specific funding information was provided for this manuscript. This section should be updated according to the target journal requirements.

Conflict of interest: The authors declare no known competing financial interests or personal relationships that could have appeared to influence the work reported in this paper.

Data availability: Processed datasets are available from the corresponding author on reasonable request. Raw instrumental files include XRD, FTIR, UV-Visible, PL and VSM data used for the analysis.

Author contributions: Bhabataran Bhakat contributed to synthesis, characterization, data analysis and manuscript preparation. Dr. Manoranjan Bar contributed to supervision, scientific interpretation and manuscript revision.

Ethical approval: Not applicable. This work does not involve human participants, animals or clinical samples.

References

[1] A. Goldman, *Modern Ferrite Technology* . 2006. doi: 10.1007/978-0-387-29413-1.

[2] J. Smit and H. P. J. Wijn, *Ferrites: physical properties of ferrimagnetic oxides in relation to their technical applications* . 1959.

[3] E. J. W. Verwey and E. L. Heilmann, "Physical properties and cation arrangement of oxides with spinel structures," Jan. 1947, Accessed: Jun. 2026. [Online]. Available: http://www.crystallography.net/cod/9012440.html

[4] C. N. Chinnasamy *et al.* , "Mixed spinel structure in nanocrystallineNiFe2O4," *Physical review. B, Condensed matter* , vol. 63, no. 18, Apr. 2001, doi: 10.1103/physrevb.63.184108.

[5] C. D. B. and G. D. C., "Introduction to magnetic materials," *Materials Today* , vol. 12, no. 3, pp. 45–45, Mar. 2009, doi: 10.1016/s1369-7021(09)70091-4.

[6] B. D. Cullity and S. R. Stock, "Elements of X-Ray Diffraction -3rd ed.-," Jan. 2001, Accessed: Jun. 2026. [Online]. Available: https://library.nims.go.jp/manifestations/59591

[7] R. D. Waldron, "Infrared Spectra of Ferrites," *Physical Review* , vol. 99, no. 6, pp. 1727–1735, Sep. 1955, doi: 10.1103/physrev.99.1727.

[8] H. Noei, H. Qiu, Y. Wang, E. Löffler, C. Wöll, and M. Muhler, "The identification of hydroxyl groups on ZnO nanoparticles by infrared spectroscopy," *Physical Chemistry Chemical Physics* , vol. 10, no. 47, pp. 7092–7092, Jan. 2008, doi: 10.1039/b811029h.

[9] R. Borah *et al.* , "Selectivity in the Ligand Functionalization of Photocatalytic Metal Oxide Nanoparticles for Phase Transfer and Self-Assembly Applications," *arXiv (Cornell University)* , vol. 27, no. 35, pp. 9011–9021, Apr. 2021, doi: 10.1002/chem.202100029.

[10] L. P. Wang, "High performance metal oxides for energy storage applications," Jul. 21, 2017. Accessed: Feb. 2026. [Online]. Available: http://www.theses.fr/2017GREAI031/document

[11] C. P. E. Varsamis, N. Makris, C. Valvi, and E. I. Kamitsos, "Short-range structure, the role of bismuth and property–structure correlations in bismuth borate glasses," *Physical Chemistry Chemical Physics* , vol. 23, no. 16, pp. 10006–10020, Jan. 2021, doi: 10.1039/d1cp00301a.

[12] A. Namai *et al.* , "Hard magnetic ferrite with a gigantic coercivity and high frequency millimetre wave rotation," *Nature Communications* , vol. 3, no. 1, pp. 1035–1035, Sep. 2012, doi: 10.1038/ncomms2038.

[13] P. Qiu, C. Jensen, N. Charity, R. A. Towner, and C. Mao, "Oil Phase Evaporation-Induced Self-Assembly of Hydrophobic Nanoparticles into Spherical Clusters with Controlled Surface Chemistry in an Oil-in-Water Dispersion and Comparison of Behaviors of Individual and Clustered Iron Oxide Nanoparticles," *Journal of the American Chemical Society* , vol. 132, no. 50, pp. 17724–17732, Nov. 2010, doi: 10.1021/ja102138a.

[14] F. Nasirpouri *et al.* , "Microstructure, ion adsorption and magnetic behavior of mesoporous γ-Fe2O3 ferrite nanoparticles," *RSC Advances* , vol. 13, no. 36, pp. 25140–25158, Jan. 2023, doi: 10.1039/d3ra01663c.

[15] V. Tong and K. P. Mingard, "Measurement uncertainties of energy dispersive X-ray spectroscopy in the scanning electron microscope (SEM-EDX/EDS)," Mar. 2026. doi: 10.47120/npl.mat135.

[16] D. E. Newbury and N. W. M. Ritchie, "Performing elemental microanalysis with high accuracy and high precision by scanning electron microscopy/silicon drift detector energy-dispersive X-ray spectrometry (SEM/SDD-EDS)," *Journal of Materials Science* , vol. 50, no. 2, pp. 493–518, Nov. 2014, doi: 10.1007/s10853-014-8685-2.

[17] R. Buonsanti and D. J. Milliron, "Chemistry of Doped Colloidal Nanocrystals," *Chemistry of Materials* , vol. 25, no. 8, pp. 1305–1317, Mar. 2013, doi: 10.1021/cm304104m.

[18] D. Chen, R. Viswanatha, G. L. Ong, R. Xie, M. Balasubramaninan, and X. Peng, "Temperature Dependence of 'Elementary Processes' in Doping Semiconductor Nanocrystals," *Journal of the American Chemical Society* , vol. 131, no. 26, pp. 9333–9339, Jun. 2009, doi: 10.1021/ja9018644.

[19] J. A. Small, "The analysis of particles at low accelerating voltages (<= 10 kV) with energy dispersive x-ray spectroscopy (EDS)," *Journal of Research of the National Institute of Standards and Technology* , vol. 107, no. 6, pp. 555–555, Nov. 2002, doi: 10.6028/jres.107.047.

[20] S. Rades *et al.* , "High-resolution imaging with SEM/T-SEM, EDX and SAM as a combined methodical approach for morphological and elemental analyses of single engineered nanoparticles," *RSC Advances* , vol. 4, no. 91, pp. 49577–49587, Oct. 2014, doi: 10.1039/c4ra05092d.

[21] K. Manthiram and A. P. Alivisatos, "Tunable Localized Surface Plasmon Resonances in Tungsten Oxide Nanocrystals," *Journal of the American Chemical Society* , vol. 134, no. 9, pp. 3995–3998, Feb. 2012, doi: 10.1021/ja211363w.

[22] T. Nguyen-Phan *et al.* , "Visible Light-Driven H2 Production over Highly Dispersed Ruthenia on Rutile TiO2 Nanorods," *ACS Catalysis* , vol. 6, no. 1, pp. 407–417, Dec. 2015, doi: 10.1021/acscatal.5b02318.

[23] I. Becerril-Romero *et al.*, "Transition-Metal Oxides for Kesterite Solar Cells Developed on Transparent Substrates," *Zenodo (CERN European Organization for Nuclear Research)* , vol. 12, no. 30, pp. 33656–33669, Jul. 2020, doi: 10.1021/acsami.0c06992.

[24] G. Wang, R. van den Berg, C. de M. Donegá, K. P. de Jong, and P. E. de Jongh, "Silica-supported Cu2O nanoparticles with tunable size for sustainable hydrogen generation," *Applied Catalysis B: Environmental* , vol. 192, pp. 199–207, Mar. 2016, doi: 10.1016/j.apcatb.2016.03.044.

[25] F. Hellman *et al.*, "Interface-induced phenomena in magnetism," *Reviews of Modern Physics* , vol. 89, no. 2, Jun. 2017, doi: 10.1103/revmodphys.89.025006.

[26] M. Ziese, "Extrinsic magnetotransport phenomena in ferromagnetic oxides," *Reports on Progress in Physics*, vol. 65, no. 2, pp. 143–249, Jan. 2002, doi: 10.1088/0034-4885/65/2/202.

[27] "Magnetism and the chemical bond," *Journal of the Franklin Institute* , vol. 276, no. 4, pp. 337–337, Oct. 1963, doi: 10.1016/0016-0032(63)90467-8.

[28] M. L. Néel, "Propriétés magnétiques des ferrites ; ferrimagnétisme et antiferromagnétisme," *Annales de Physique* , vol. 12, no. 3, pp. 137–198, Jan. 1948, doi: 10.1051/anphys/194812030137.

[29] J. Tauc, *Amorphous and Liquid Semiconductors*. 1974. doi: 10.1007/978-1-4615-8705-7.

[30] K. Maaz, A. Mumtaz, S. K. Hasanain, and A. Ceylan, "Synthesis and magnetic properties of cobalt ferrite (CoFe2O4) nanoparticles prepared by wet chemical route," *arXiv (Cornell University)* , vol. 308, no. 2, pp. 289–295, Jul. 2006, doi: 10.1016/j.jmmm.2006.06.003.

[31] Q. Song and Z. J. Zhang, "Shape Control and Associated Magnetic Properties of Spinel Cobalt Ferrite Nanocrystals," *Journal of the American Chemical Society* , vol. 126, no. 19, pp. 6164–6168, Apr. 2004, doi: 10.1021/ja049931r.

[32] C. Sun, J. Lee, and M. Zhang, "Magnetic nanoparticles in MR imaging and drug delivery," *Advanced Drug Delivery Reviews*, vol. 60, no. 11, pp. 1252–1265, Apr. 2008, doi: 10.1016/j.addr.2008.03.018.

[33] B. Bhakat and M. Bar, "The Structural, Vibrational, Morphological, Optical, and Magnetic Property Studies of Nickel-Doped Manganese Ferrite ($Ni_{0.3}Mn_{0.7}Fe_2O_4$) Nanoparticles," *International Journal of Science and Technology (IJST)*, vol. 3, no. 2, pp. 257–269, Jun. 2026, doi: 10.70558/ijst.2026.v3.i2.241278.

[34] S. Chikazumi and C. D. Graham, *Physics of Ferromagnetism* . 1997. doi: 10.1093/oso/9780198517764.001.0001.

[35] R. M. Cornell and U. Schwertmann, *The iron oxides: structure, properties, reactions, occurrences and uses.* 2003, p. 2664. doi: 10.1002/3527602097.

[36] H. M. Rietveld, "A profile refinement method for nuclear and magnetic structures," *Journal of Applied Crystallography*, vol. 2, no. 2, pp. 65–71, Jun. 1969, doi: 10.1107/s0021889869006558.